


RESEARCH

Open Access



# Confocal nonlinear optical imaging on hexagonal boron nitride nanosheets

Gwanjin Lee<sup>1</sup>, Konkada Manattayil Jyothsna<sup>2</sup>, Jonghoo Park<sup>3</sup>, JaeDong Lee<sup>1</sup>, Varun Raghunathan<sup>2</sup> and Hyunmin Kim<sup>4,5\*</sup> 

\*Correspondence:

hyunmin.kim@dgjst.ac.kr

<sup>1</sup> Department of Physics and Chemistry, DGIST, Daegu 42988, Republic of Korea

<sup>2</sup> Department of Electrical Communication Engineering, Indian Institute of Science, Bangalore, India

<sup>3</sup> School of Electronics Engineering, Kyungpook National University, Daegu 41566, Republic of Korea

<sup>4</sup> Division of Biotechnology, DGIST, Daegu 42988, Republic of Korea

<sup>5</sup> Department of Interdisciplinary Engineering, DGIST, Daegu 42988, Republic of Korea

## Abstract

Optical microscopy with optimal axial resolution is critical for precise visualization of two-dimensional flat-top structures. Here, we present sub-diffraction-limited ultrafast imaging of hexagonal boron nitride (hBN) nanosheets using a confocal focus-engineered coherent anti-Stokes Raman scattering (cFE-CARS) microscopic system. By incorporating a pinhole with a diameter of approximately 30  $\mu\text{m}$ , we effectively minimized the intensity of side lobes induced by circular partial pi-phase shift in the wavefront (diameter,  $d_0$ ) of the probe beam, as well as nonresonant background CARS intensities. Using axial-resolution-improved cFE-CARS (acFE-CARS), the achieved axial resolution is 350 nm, exhibiting a 4.3-folded increase in the signal-to-noise ratio compared to the previous case with 0.58  $d_0$  phase mask. This improvement can be accomplished by using a phase mask of 0.24  $d_0$ . Additionally, we employed nondegenerate phase matching with three temporally separable incident beams, which facilitated cross-sectional visualization of highly-sample-specific and vibration-sensitive signals in a pump-probe fashion with subpicosecond time resolution. Our observations reveal time-dependent CARS dephasing in hBN nanosheets, induced by Raman-free induction decay (0.66 ps) in the 1373  $\text{cm}^{-1}$  mode.

**Keywords:** Hexagonal boron nitride nanosheets, Sub-diffraction-limited nonlinear optical microscopy, Coherent anti-Stokes Raman spectroscopy, 2D materials, Ultrafast phonon dynamics

## Introduction

Hexagonal boron nitride (hBN) crystals, traditionally utilized as heat- or wear-resistant bulk ceramics, have recently been researched because of their superior optoelectronic properties that critically develop in the shape of atomically thin sheets [1]. The alternative hexagonal planar occupations of boron and nitrogen atoms effectively prevent the possible formation of surface roughness or defects during the fabrication of 2D hBN nanosheets, allowing excellent passivation of charge traps, which otherwise create unwanted chemical reactions or electrical leakage [2–5]. Under heterogeneous integration with other van der Waals crystals, the photoelectric stability of the hybrid structures also plays a critical role in the efficient generation of surface plasmons or phonon polaritons for better light-emitting applications [6–9]. The lithographically patterned hBN

structure successfully served as a high-Q mid-IR light source, which generated deep UV (DUV) emission and paved the way for various DUV-driven hBN-integrated photonic devices [10–12]. Schematically designed Schottky defects formed in honeycomb structures (analogous to nitrogen defects in diamonds) have also been frequently mentioned as a single-photon source for quantum information transport [13–15].

The nonlinear optical properties of 2D hBN are presently garnering attention, similar to other transition metal dichalcogenide materials, because of its high nonlinear optical light conversion efficiency achieving phase-matching conditions from its atomically thin nature in thickness [16]. The second harmonic generation (SHG) of a single-layered hBN sheet was first reported to be more efficient than a quartz substrate by one order of magnitude [17]. Simultaneously, it is two orders of magnitude smaller than that of MoS<sub>2</sub>. The thickness dependence of the SHG contrast follows an odd parity rule due to the existence of centrosymmetry with an increase in the layer number. In addition, the third-order nonlinear optical susceptibility ( $\chi^{(3)}$ ) of hBN nanosheets was investigated, and the mechanism of the phonon-exciton coupled radiation of DUV light was detailed using photoluminescence measurements [18–21]. The in-plane E<sub>2g</sub> vibration mode of hBN nanosheets is critically assessed by coherent anti-Stokes Raman spectroscopy and stimulated Raman microscopy [22, 23]. Most recently, the third harmonic generation of bulkier (5–170 nm) hBN nanosheets was rigorously assessed with a value of  $8.4 \times 10^{-21} \text{ m}^2/\text{V}^2$ , an order of magnitude higher than that of fused silica [21].

Moreover, as the size of future electronic devices decreases, it is necessary to improve the visualization of the physicochemical functions of nanocrystalline systems in the axial and lateral directions. Motivated by this background, we performed axial-resolution-improved confocal focus-engineered CARS (acFE-CARS) microscopy to characterize exfoliated planar hexagonal boron nitride (hBN) nanosheets. The z-directional resolution ranges from approximately 1.6  $\mu\text{m}$  to approximately 350 nm by sacrificing the lateral resolution from approximately 96 nm to approximately 120 nm. The optimized 3D configuration of the point spread function requires resetting of the phase mask size from 0.58  $d_0$  to 0.24  $d_0$  under a similar pinhole size of 30  $\mu\text{m}$ ; accordingly, a more stringent confocal condition with an otherwise low signal-to-noise (SNR) level was guaranteed. This approach effectively improved the axial resolution and removed the nonresonant background signals from the substrate. The chemical sensitivity of acFE-CARS for hBN nanosheets was compared with that of Raman spectroscopy and the theoretical model. The enhancement in edge resolution correlated well with atomic force microscopy (AFM).

## Results and discussion

### Nondegenerate epi-CARS of hBN nanosheets

The hexagonal boron nitride (hBN) system is an electrically insulating material with a wide bandgap of up to 5.96 eV, allowing no electronic resonance condition of any three wavelengths ( $\omega_1$  for 910 nm,  $\omega_2$  for 1040 nm, and  $\omega_3$  for 455 nm) here. The distances between the red dotted lines in Fig. 1a are proportional to the real energy values referenced from the energy diagram by first-principles calculations. A CARS field (purple) is generated by probing action ( $\omega_3$  for 455 nm, blue) for the phonon mode (E<sub>2g</sub>, 1366  $\text{cm}^{-1}$ ) beaten by the pump ( $\omega_1$  for 910 nm) and Stokes ( $\omega_2$  for 1040 nm) beams. In addition, the energy conservation

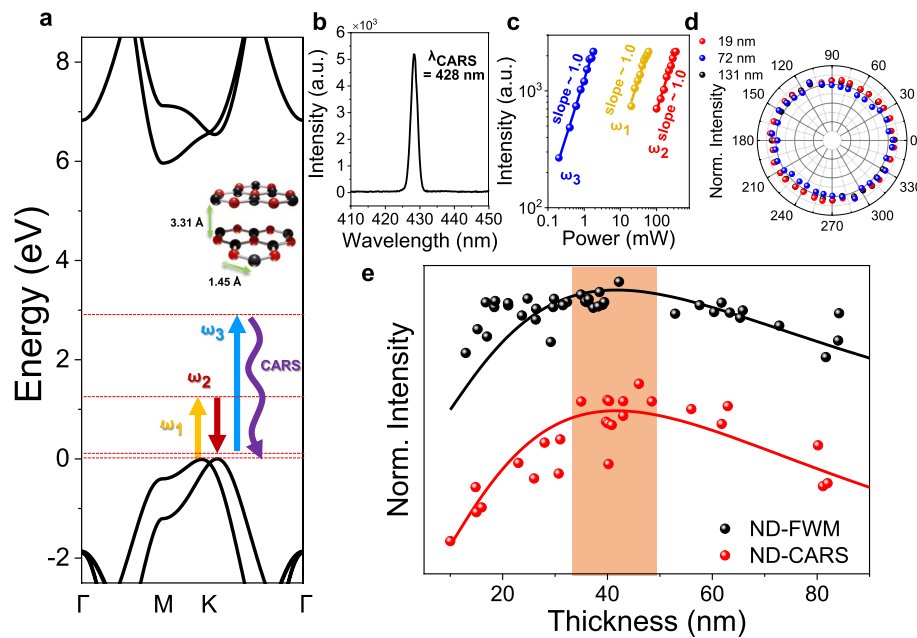


**Fig. 1** **a** The nondegenerate (ND) CARS process indicated on the energy diagram of bulk hexagonal boron nitride (hBN), where  $\omega_1$  is 910 nm,  $\omega_2$  is 1040 nm, and  $\omega_3$  is 455 nm. **b** The spectrum of ND-CARS from hBN flakes. **c** The power dependence of ND-CARS from hBN flakes. **d** The polarization dependence of ND-CARS from hBN flakes. **e** Four-wave mixing ( $\omega_1$ , 810 nm;  $\omega_2$ , 1040 nm;  $\omega_3$ , 405 nm; black) and ND-CARS ( $\omega_1$ , 910 nm;  $\omega_2$ , 1040 nm;  $\omega_3$ , 455 nm; red) intensity as a function of the thickness of hBN flakes

of CARS ( $\hbar\omega_{\text{CARS}} = \hbar\omega_1 - \hbar\omega_2 + \hbar\omega_3$ ) asserts that the wavelength of the generated CARS field is 428 nm (Fig. 1b). Generally, the intensity ( $I_{\text{CARS}}$ ) of ND-CARS with third-order susceptibility ( $\chi^{(3)}$ ) is expressed as a function of the pump ( $\omega_1$ ), Stokes ( $\omega_2$ ), and probe ( $\omega_3$ ) intensities along the sample thickness  $z$  as follows [24]:

$$I_{\text{ND-CARS}} \propto \left| \chi^{(3)} \right|^2 I_{\text{pu}} I_{\text{pr}} I_s \left[ \frac{\sin^2 \left( z \cdot \frac{\Delta k}{2} \right)}{\left( \frac{\Delta k}{2} \right)^2} \right] \quad (1)$$

where  $I_{\text{pu}}$ ,  $I_s$  and  $I_{\text{pr}}$  are the pump, Stokes, and probe intensities, respectively.  $\Delta k$  represents the phase difference, explaining the linear dependence on the input power of each beam in Fig. 1c. In Fig. 1d, the polarization dependence (sample rotation) of ND-CARS was determined for three nanosheets with different thicknesses. We confirmed that the isotropic symmetric property of the  $E_{2g}$  vibration is consistent with that measured by stimulated Raman scattering imaging [22]. Given the meticulous correlation of the exfoliated hBN nanosheets with the optical image and ND-CARS microscopy, the dependence of the CARS intensity on the thickness is summarized in Fig. 1e. Generally, the coherence length of the CARS is expressed with regard to the backward (plus) and forward (minus) directions as follows [25, 26]:

$$l_{\text{coh}} = \frac{\pi}{\Delta k} = \frac{\pi}{n_{\text{CARS}} \frac{2\pi}{\lambda_{\text{CARS}}} \pm \left( n_{\text{pu}} \frac{2\pi}{\lambda_{\text{pu}}} + n_{\text{pr}} \frac{2\pi}{\lambda_{\text{pr}}} - n_s \frac{2\pi}{\lambda_s} \right)} \quad (2)$$

where  $n_{\text{CARS}}$ ,  $n_{\text{pu}}$ ,  $n_{\text{pr}}$ , and  $n_s$  are the refractive indices of the CARS, pump, probe, and Stokes beams, respectively, and  $\lambda_{\text{CARS}}$ ,  $\lambda_{\text{pu}}$ ,  $\lambda_{\text{pr}}$ , and  $\lambda_s$  are the beam wavelengths. Based on the above model, the coherent length of the ND-CARS tuned to the  $E_{2g}$  band is 47 nm (red dots;  $\omega_1$ , 910 nm;  $\omega_2$ , 1040 nm;  $\omega_3$ , 455 nm), of which one of the nonresonant ND-CARSs (black dots;  $\omega_1$ , 810 nm;  $\omega_2$ , 1040 nm;  $\omega_3$ , 405 nm) is 39 nm. This trend is reflected in the data in the form of maximum intensity in the shadowed area<sup>21</sup>. The coherent lengths of the forward ND-CARS corresponding to the above cases are approximately 10 and 4  $\mu\text{m}$ . From the modified relation of Eq. 1, for the sinc function, the CARS contrast for the 2D material system quadratically increased until around the tenth layer and gradually decreased as the layers ( $z$ ) were incremented. This is attributed to the transmittance change in the electric field related to intrasystematic absorption [27]. We adopted the theoretical CARS intensity for  $N$ -layered graphene for a more quantitative analysis. It was modeled as  $N^2/(1 + N \cdot 2\pi\sigma/c)^8$ , where  $\sigma$  and  $c$  are the optical conductivity and speed of light, respectively [28]. The experimental results agree well with the theoretical modeling. The optical conductance achieved via fitting was  $1.7 \times 10^{-5} \Omega^{-1}$ , approximately three times lower than that of graphene ( $6.08 \times 10^{-5}$ ). Here, no clear evidence of phonon enhancement in the optical conductance was observed.

#### Ultrafast phonon dynamics of hBN nanosheets measured by ND-CARS

The susceptibility of the hBN system ( $\chi_{\text{hBN}}^{(3)}$ ) in the near vibration mode ( $\omega_v$ ) can be approximated as  $A_v/(\omega_v - (\omega_1 - \omega_2) - i\Gamma_v) + \chi_{\text{NR}}^{(3)}$ , where  $A_v$  is a factor for the Raman scattering cross-section,  $\Gamma_v$  is the linewidth of the vibration mode, and  $\chi_{\text{NR}}^{(3)}$  is the nonresonant CARS (abbreviated as ND-FWM here) susceptibility [29]. Figure 2a illustrates the principle of obtaining the coherency (built by  $\omega_1 - \omega_2$ ) of the damped molecular vibration via time-resolved CARS spectroscopy as a function of the time delay ( $\tau$ ) of the probe pulse. The vibrational frequency of hBN was not readable because it was much faster ( $1366 \text{ cm}^{-1} = 24 \text{ fs}$ ) than the pulse width (120 fs). Figure 2b shows the pulse envelope, approximately half ( $428 \text{ cm}^{-1} = 78 \text{ fs}$ ) of the FWHM of the superimposed pulse width, which overlaps with the  $E_{2g}$  mode of the Raman spectrum of the hBN flakes. The thicknesses of the studied hBN nanosheets ranged from 20 to 100 layers and did not exhibit any significant sample-to-sample differences from  $1366 \text{ cm}^{-1}$  [30]. Here, the linewidth of the vibration mode was measured to be  $10 \text{ cm}^{-1}$  deconvolved with  $7.78 \text{ cm}^{-1}$ , corresponding to a 0.68 ps dephasing time ( $T_2/2 = 2\hbar/\Gamma_R$ ) [31–33]. Time-resolved ND-CARS and ND-FWM microscopy [34] images for Fig. 2c–e and time-resolved dynamics were collected for the green dashed circle area in Fig. 2d–e. The time-resolved CARS dynamics consist of the instrumental response function (IRF) associated with the cross-correlation between three pulses and coherent anti-Stokes Raman scattering from  $E_{2g}$  vibration (see Methods) [32, 33]. The Raman free-induction decay ( $T_2/2 = 0.66 \text{ ps}$ ) is measured by time-resolved ND-CARS which is consistent with the lifetime obtained from the spontaneous Raman spectrum ( $T_2/2 = 0.68 \text{ ps}$ ). Because of photodamage, limited power (approximately 5.32 mW, 14.45 mW, and 0.15 mW for  $\omega_1$ ,  $\omega_2$ , and  $\omega_3$ , respectively) dependence measurements were allowed from 1 to 4.8 mW, as with the pump and Stokes beams. This demonstrates a small contrast inversion (between 3 and 4 in Fig. 2e), presumably due to the inertial intermolecular response [35, 36]. Fig. 2f–g show the time-resolved CARS spectra as functions of the probe delay of arbitrarily

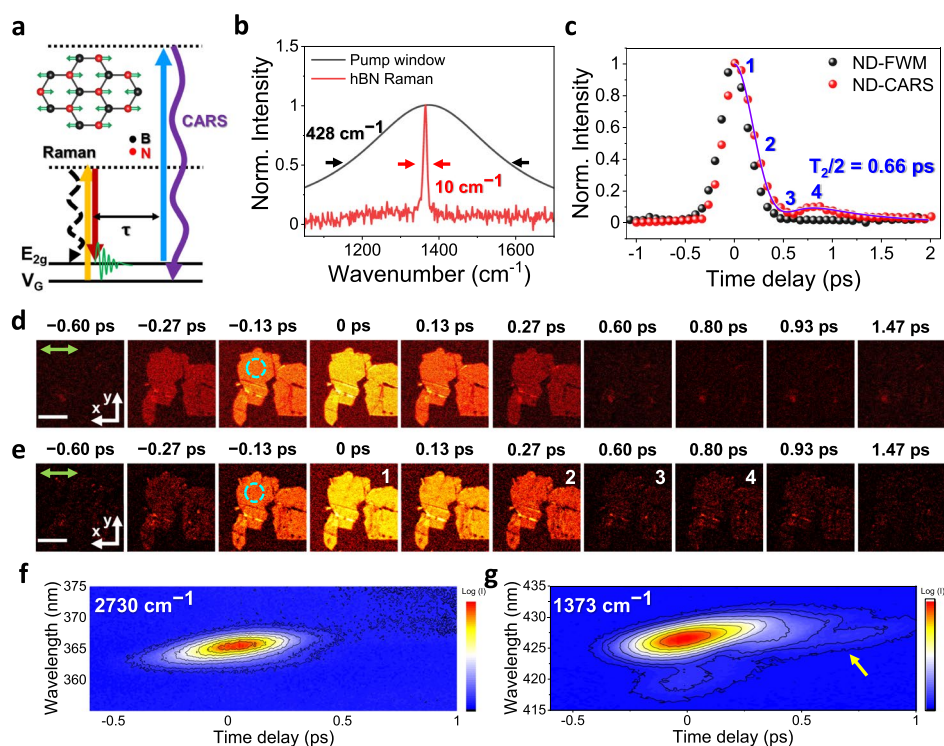


**Fig. 2** **a** Schematic of the ND-CARS process of hBN **b** Raman spectrum of hBN and spectrum window of pump pulses **c** Time-resolved ND-CARS ( $\omega_1$ , 910 nm;  $\omega_2$ , 1040 nm;  $\omega_3$ , 455 nm) and ND-FWM ( $\omega_1$ , 810 nm;  $\omega_2$ , 1040 nm;  $\omega_3$ , 405 nm) of hBN flakes. The intensities are collected from time-resolved **d** ND-FWM ( $\omega_1$ , 810 nm;  $\omega_2$ , 1040 nm;  $\omega_3$ , 405 nm) and **e** ND-CARS ( $\omega_1$ , 910 nm;  $\omega_2$ , 1040 nm;  $\omega_3$ , 455 nm) images of hBN (cyan dotted circles). Time-resolved spectrum of **f** ND-FWM ( $\omega_1$ , 810 nm;  $\omega_2$ , 1040 nm;  $\omega_3$ , 405 nm) and **g** ND-CARS ( $\omega_1$ , 910 nm;  $\omega_2$ , 1040 nm;  $\omega_3$ , 455 nm) of hBN. The green arrows indicate the polarization direction. A logarithmic scale is used for **d–g**. The white scale bars correspond to 6  $\mu\text{m}$

thick hBN nanosheets. Figure 2g was obtained using 910 nm/1040 nm as pump/Stokes beams, which were ascribed to the  $E_{2g}$  phonon mode of hBN crystals, and 455 nm as the probe beam to generate a CARS beam at 428 nm. The pulse envelope covered by a pump (120 fs) and probe (220 fs) was calculated as approximately 78 fs with a center at 1373  $\text{cm}^{-1}$  [37]. In contrast, Fig. 2f was obtained using 810 nm/1040 nm/405 nm as pump/Stokes/probe beams, which detected phonon vibrations at approximately 2730  $\text{cm}^{-1}$ . The appearance of oscillatory tails in Fig. 2f demonstrates a clear difference between the two spectra, which is consistent with the image data (Fig. 2c–e).

### Focal size configuration in cFE-CARS microscopy

The optical resolution has been improved by reducing the lateral focal width using a pinhole, more specifically by cutting off the side-lobe volume caused by destructive interference originating from the partial phase delay of the wavefront of the probe beam [38–40]. Figure 3a shows a complete illustration of the optical path of the cFE-CARS microscope. Briefly, an optical parametric oscillating Yb-doped fiber laser emits a pair of femtosecond pulses, one of which is a fundamental mode ( $\omega_2$ , 80 MHz, FWHM 220 fs). The other is a wavelength variant (680–1300 nm) mode ( $\omega_1$ , FWHM 120 fs). Here,  $\omega_1$  is frequency doubled to  $\omega_3 (= 2\omega_1)$  by the BBO crystal and is directed



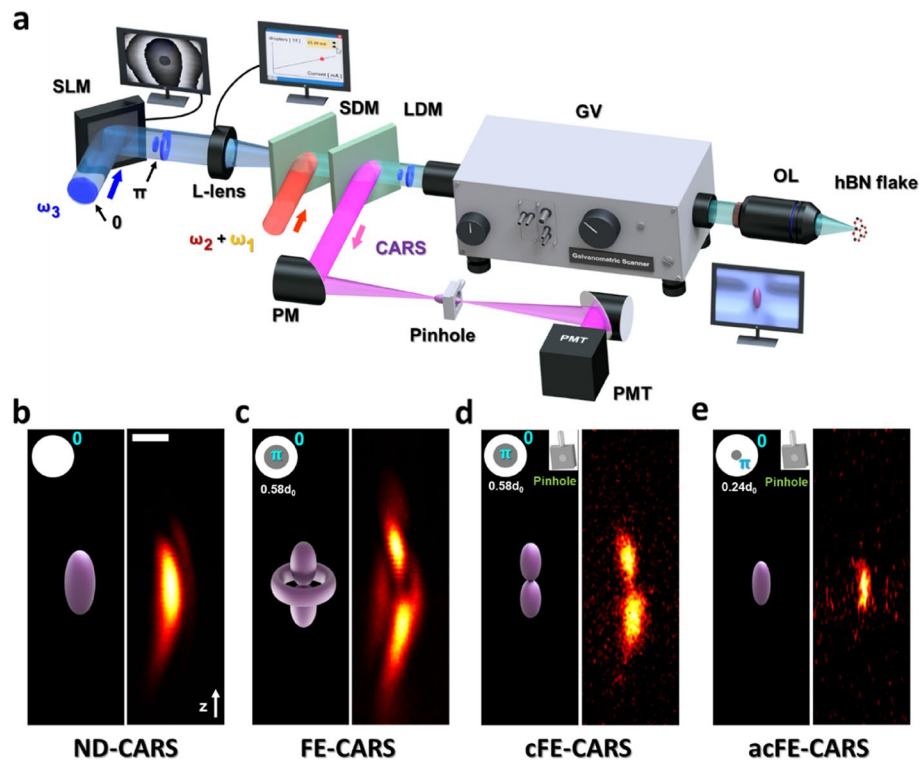


**Fig. 3** **a** Schematic of confocal focus-engineered CARS microscopy. SLM, spatial light modulator; L-lens, liquid lens; SDM, short pass dichroic mirror; LDM, long pass dichroic mirror; OL, objective lens; GV, galvanometric mirror; PM, parabolic mirror; PMT, photomultiplier tube. The z-directional point-spread functions for **b** ND-, **c** FE-, **d** cFE-, and **e** acFE-CARS. The circular phase mask patterns and pinhole presence are illustrated as insets with the respective illustrated focal shapes. The white scale bar corresponds to 500 nm

to the spatial light modulator (SLM) for a subsequent focus engineering process. In SLM, the background-corrected circular patterns of the phase masks are encoded from  $\pi$ , freely offering a partial  $\pi$  phase delay in the central portion. The chromatic aberration among the three waves was corrected using a liquid lens (L-lens) in the  $\omega_3$  pathway. After passing the SLM and L-lens, the  $\omega_3$  wave is overlapped to the  $\omega_1$  and  $\omega_2$  fields using a “short pass” dichroic mirror and finally focused using an objective lens in the imaging system. The focus-engineered (FE) CARS signals are bounced back to the galvanometric (GV) scanner. They are then redirected via a “long pass” dichroic mirror (LDM) to the external photomultiplier tube (PMT) detector. Before the final detection, the FE-CARS beam was refocused using a pair of parabolic mirrors to obtain confocal geometry from the sample focal plane. The focused beam is filtered out via a  $30\ \mu\text{m}$  pinhole to remove the side lobes and the background signals out of the confocal position from the pinhole to eventually improve the z-directional resolution [41]. The focal shape of axially adjusted confocal focus-engineered CARS (acFE-CARS) microscopy is sequentially compared with other CARS techniques from Fig. 3b–e. Figure 3b shows a z-directional scan of an isolated ZnO nanoparticle taken by ND-CARS, where no phase-mask image is applied to the wavefront of the  $\omega_3$  field, which drastically changes with the application of the phase mask ( $d = 0.58d_0$ ) in FE-CARS in Fig. 3b. The average diameter in the central lobe was carefully determined to

be 110 nm and was improved to approximately 87 nm with the application of pinholes in the detection line (cFE-CARS), as thoroughly examined before [38]. However, the marginal signal-to-noise level (10–30) hampered the applicability of our work, forcing us to enhance the absolute CARS contrast by reducing the area of the central  $\pi$  phase delay mask (from 0.58 to 0.24  $d_0$ ) in the presence of the pinhole. In this way, we were permitted to obtain the final point spread, as shown in Fig. 3e, with a sacrifice of a lateral resolution of 120 nm and a drastic improvement in the axial resolution up to 350–500 nm (using hBN nanosheets, Fig. 4) in acFE-CARS microscopy.

### The optical resolution of acFE-CARS microscopy

An arbitrary region with a few exfoliated hBN nanosheets (of different thicknesses) was chosen to assess the spatial resolution of the acFE-CARS microscopy, as shown in Fig. 4a. Fig. 4b–c show the xy-directional ND- and acFE-CARS images of the hBN nanosheets, indicated by the green dashed box in Fig. 4a. We selected thin (approximately 19 nm) flakes (at the central part of the green box in Fig. 3a), which were measured by AFM (Supplementary Fig. 11b) to critically evaluate the resolution of acFE-CARS for hBN systems. Fig. 4b–c shows the ND- and acFE-CARS xy-directional images of the thin hBN

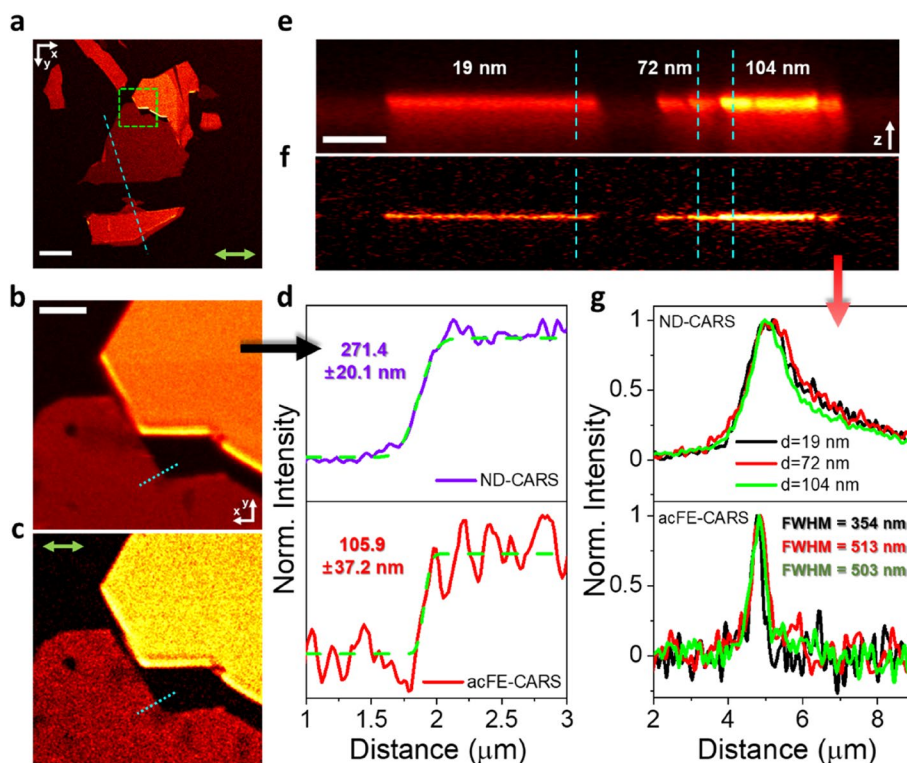


**Fig. 4** **a** The xy-directional image of ND-CARS ( $\omega_1$ , 910 nm;  $\omega_2$ , 1040 nm;  $\omega_3$ , 455 nm) of hBN flakes. The xy-directional mean filtered images of **b** ND-CARS and **c** acFE-CARS ( $\omega_1$ , 910 nm;  $\omega_2$ , 1040 nm;  $\omega_3$ , 455 nm) of hBN flakes, whose region is indicated with a green box in **a**. **d** The line profiles of ND-CARS and cFE-CARS of hBN are shown with cyan dotted lines in **b** and **c**. The line profiles are fitted with a Gaussian cumulative distribution function. The distance between 10 and 90% of fitted function is indicated in **f**. The z-directional mean filtered image of **e** ND-CARS and **f** acFE-CARS of hBN of which region is indicated with cyan dashed line in **a**. **g** The z-directional line profiles of ND-CARS and acFE-CARS of hBN flakes whose region is indicated with cyan dashed lines in **e** and **f**. The green arrows indicate the polarization direction. The white scale bars correspond to **a** 10  $\mu\text{m}$ , **b** 2  $\mu\text{m}$ , and **e** 5  $\mu\text{m}$

nanosheets. The contrast of the ND-CARS image was noticeably blurrier than that of the acFE-CARS image, showing a smaller field of view in the gap area composed of the upper part of the target hBN flake and the lower part of the thick one. Specifically, more discernible contrast enhancement on the edge side was assessed with a line profile drawn along the lines in Fig. 4b–c for more quantitative analysis, of which edge resolution was performed by measuring the distance between 10 and 90% from the maximum intensity along the line profiles [42–44]. The summarized intensity comparison among the different techniques in Fig. 4d reveals that the actual edge slope length can be resolved via acFE-CARS at 105.9 nm. In contrast, the same distance can be determined via ND-CARS microscopy at 271.4 nm. Thus, acFE-CARS is more than twice as effective. These numbers in the edge resolutions of ND- and acFE-CARS are compared with those of AFM in Supplementary Fig. 8.

However, the z-directional resolution was elucidated by axial scanning along the lime-dashed line in Fig. 4a. Axial image scanning was performed using the ND and acFE-CARS methods, as shown in Fig. 4e and 4f, respectively. In Fig. 4e, the z-directional CARS contrast from hBN is blurry and mixed with that from the background signal at the interface of the coverslip glass, which becomes more severe as the thickness of the hBN nanosheet increases. However, the z-directional image obtained by the acFE-CARS technique shows sharper and narrower contrasts for all the considered thicknesses (19, 72, and 104 nm) of the hBN nanosheets (Fig. 4f). For more information, the z-directional optical resolution ( $\mathcal{R}_z$ ) of coherent light-scattering systems is defined as follows [45, 46]:

$$\mathcal{R}_z = \frac{2n\lambda}{NA^2} \quad (3)$$

where  $\lambda$  is the wavelength of the excitation light,  $n$  is the refractive index in the objective plane, and  $NA$  is the numerical aperture of the objective lens. The above equation implies that the usage of index matching materials with a higher refractive index inherently worsens the z-directional resolution. The theoretical FWHM of axial ND-CARS microscopy is approximately 913 nm (based on the assumption of 455 nm excitation, see Supplementary Fig. 5), which is already massively exaggerated by the mixed contributions of optical misalignment and background contamination up to the approximately 2  $\mu\text{m}$  scale according to the Gaussian-fitted full width at half maximum (FWHM) values in the upper part of Fig. 4g. In contrast, the  $\mathcal{R}_z$  of the acFE-CARS microscopy was improved to 350 nm in the thinnest sheets, as demonstrated in the upper part of the line profile graphs in Fig. 4g, confirming the sub-diffraction-limited nature of the acFE-CARS system. Generally, the technical challenges for z-directional resolution advancement have been extensively sought by collecting the fluorescence signals in a 90° angled objective lens in 4PI microscopy or light sheet microscopy. Remarkably, the high quantum yield fluorescence signals of fluorophores generated from z-directionally formed standing wave illumination were schematically utilized for approximately twice the axial resolution in widefield structured illumination microscopy.

#### Axial time-dependent acFE-CARS microscopy

In CARS microscopy, nonresonant signals from the substrate and even from immersive oil or water deteriorate the quality of the original contrast. Thus, heterodyne



detection with CARS photons generated from other sources or modulated frequency detection of the pump by the probe beam (or vice versa), as in stimulated Raman scattering microscopy, has been frequently adopted for better background-free images [47, 48]. Fig. 5a–b show a few selected time-resolved acFE-CARS images as a function of probe delay scanned in the lateral and axial directions. The pulse envelope covered by the pump (120 fs) and probe (220 fs) was calculated at approximately 78 fs with the center at  $1373\text{ cm}^{-1}$  [37]. Similar to the image sets in Fig. 2b, the CARS contrasts re-raised between Images 3 (0.6 ps of probe delay) and 4 (0.8 ps), presumably caused by phonon–phonon scattering only in the hBN specimen, which is not shown in the glass substrate. A more drastic demonstration of the suppression of the background CARS is shown in Fig. 5c, where ND-CARS resolves the z-directional time-resolved phonon dynamics. Here, the nonvibrational-mode CARS signals from glass and immersion oil gradually disappear (green arrow), whereas the  $E_{2g}$  mode of hBN phonons is highly scattered and creates a subsequent resurrection of CARS signals (blue arrow). Figure 5c compares the time-dependent changes in the CARS signals taken from Fig. 5a (blue), 5b (blue), and 5c (green) from the hBN nanosheets. The CARS contrasts were re-brightened at the approximately 0.8 ps probe delay position for the hBN sample. The signal variation was not discernible for the glass substrate (such as the ZnO nanoparticle in Supplementary Fig. 6) and rather diminished.

## Conclusion

In summary, we applied an axial sub-diffraction-limited pump-probe mode confocal focus-engineered coherent anti-Stokes Raman scattering microscope to study the vibration dynamics of exfoliated hBN nanosheets. The ultrafast time-dependent measurement was achieved using an additional probe beam after doubling the pump beams. The chromatic aberration of the near UV beam was corrected with a liquid lens, which

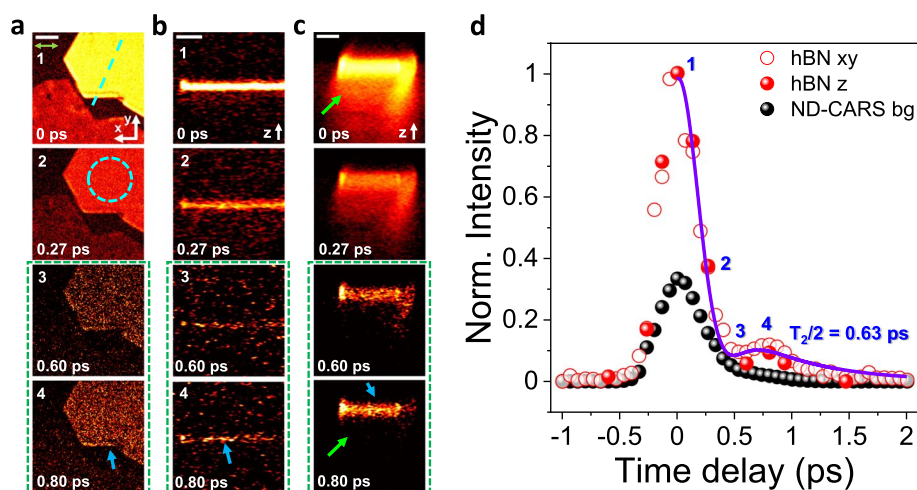


**Fig. 5** Time-resolved acFE-CARS ( $\omega_1$ , 910 nm;  $\omega_2$ , 1040 nm;  $\omega_3$ , 455 nm) **a** xy- and **b** z-directional mean filtered images of hBN flakes. **c** z-directional time-resolved ND-CARS images for an arbitrary region. **d** Time-resolved cFE-CARS dynamics from xy- and z-directional images of hBN flakes (bg, background). A logarithmic scale is used for a–c. The images in the green dashed boxes are rescaled to represent re-raised signals while maintaining the background (the empty region) level. The green arrow in a indicates the polarization direction. The white scale bars correspond to  $2\ \mu\text{m}$

resulted in more than ten times enhancement in the CARS signal [38]. To image the thin atomic layered film, the axial resolution was improved from 1.6  $\mu\text{m}$  to 350 nm with a sacrifice in the lateral resolution (from 96 to 120 nm) compared with our previous report, which is mainly made possible by reducing the phase mask diameter for better contrast. Given the revamped focal PSF in acFE-CARS microscopy, we achieved a vivid appearance of Raman-free induction decay from hBN nanosheets in axially scanned probe-delayed images compared to the glass substrate. We strongly believe that the idea to manipulate the “con-focus” of the real nonlinear optical focus can be upgraded with more diverse pinhole sizes and geometries of phase masks as a potential ultrafine platform to study the ultrafast vibrational dynamics of material and biological systems in a sub-diffraction-limited regime in a three-dimensional fashion.

## Methods

### acFE-CARS microscope

The commercial Yb-doped fiber laser (Insight DeepSee dual, Spectra Physics) supported dual-mode options of fundamental (1040 nm) and wavelength-tuning (680–1300 nm) operations, permitting the former to be used as a Stokes beam and the latter as a pump beam in two-beam CARS microscopy. The tunable part of the lasing beam was split using a 70:30 beam splitter, and the wavelength of the higher-intensity portion was halved (455 nm) using a second-harmonic generation process in a  $\beta$ -barium borate crystal (Edmond Optics). We used a circular pinhole with a diameter of 25  $\mu\text{m}$  (Newport, 900PH-25; 30  $\mu\text{m}$  diameter circular pinhole used for Supplementary Fig. 3 and Supplementary Figs. 8 and 9, Newport, 900PH-30) to correct the distorted beam shape. This shorter-wavelength beam was utilized as the probe beam in ND-CARS field generation. Additional focus matching of the probe beam was performed continuously using a liquid lens (Optotune, EL-10–30-C-VIS-LD-MV) placed in the probe beam path. Concentric circular phase control of the wavefront of the probe beam was implemented using a reflective SLM (Hamamatsu, LCOS-SLM) with a corrected flat background phase profile. Two long-focal length ( $f_1 = 1000$  mm and  $f_2 = 750$  mm) convex lenses were used to image the phase-modulated wavefront shapes from the SLM to the oil-immersion objective lens (Olympus, UplanSApo, 1.35NA, 60X, oil immersed) with a 4f geometry. The backscattered CARS photons were directed backward before the galvanometric mirror (Fluoview1200, Olympus) to achieve a spatially fixed input position (descanned detection geometry). The CARS photons were directed by dichroic mirrors (LM01-427–25 SEMROCK) and imaged onto a pinhole to obtain the confocal imaging conditions at the image planes. The two parabolic mirrors (MPD149-F01, Thorlab) and a 30  $\mu\text{m}$  circular pinhole (Newport, 900PH-30; 40  $\mu\text{m}$  diameter circular pinhole used for Supplementary Figs. 8 and 9, Newport, 900PH-40) were utilized for pinhole filtering in acFE-CARS. Three bandpass filters (Semrock) were used to select the CARS beam at 428 nm (FF01-425/26, and FF01-414/46), which was collected by a photomultiplier tube (PMT, Hamamatsu). The image collection times are approximately 10 s per image for hBN nanosheets to obtain lower laser-induced damage. The spectra were analyzed independently using a monochromator (Acton SP-2300i, Princeton Instruments) combined with a CCD camera (PIXIS 100 B, Princeton Instruments) and a 50:50 beam splitter.

### Time-resolved CARS spectroscopy

The time-resolved CARS intensity consists of the instrumental response function (IRF) associated with the cross-correlation between the three pulses and coherent anti-Stokes Raman scattering from  $E_{2g}$  vibration [31, 32]. One example of IRF is the nonresonant background (NRB) signal like four-wave mixing. In addition, CARS and NRB emit same anti-Stokes frequency at same position in hBN and interference between them could give additional effects [49–51]. Furthermore, the NRB is reported in CARS measurement probing  $E_{2g}$  vibration in hBN [22]. Therefore, we can express time-resolved CARS intensity with Eq. (4).

$$I_{\text{CARS}} \propto \left| \exp\left(-2\ln 2 \frac{t^2}{T_{\text{IRF}}^2}\right) \exp(i\omega t) + A_{\text{CARS}} \exp\left(-\frac{t-t'}{T_2}\right) \exp(i\omega(t-t')) \right|^2 \quad (4)$$

The  $T_{\text{IRF}}$  is the FWHM of the cross-correlation signal,  $T_2/2$  is Raman-free induction decay,  $A_{\text{CARS}}$  is the relative amplitude of CARS,  $\omega$  is the angular frequency of CARS, and  $t'$  is the phase mismatch between IRF and CARS signals. The first contribution is associated with IRF and the second contribution is associated with CARS signals. Then,  $T_{\text{IRF}}$  is 0.52 ps (0.38 ps, the 1/e width),  $T_2/2$  is 0.66 ps, and  $t'$  is  $0.56 \times 10^{-3}$  ps for Fig. 2c.  $T_{\text{IRF}}$  is 0.45 ps (0.32 ps, the 1/e width),  $T_2/2$  is 0.63 ps, and  $t'$  is  $0.54 \times 10^{-3}$  ps for Fig. 5d.

### Mechanical exfoliation of hBN

The hBN flakes (2D semiconductors) were poured onto a sticky side of  $\sim 20$  cm length Scotch tape (3M) which is fixed to the lab table. Then, it was repeatedly (5–6 times) exfoliated until atomically thin flakes were obtained, as reported in the literature [21, 52]. The final portion of the Scotch tape was attached to a coverslip, rubbed repeatedly with a cotton swab for 1 min, and finally the Scotch tape was detached from the coverslip. The monolayer graphene capping process is employed for the scanning electron microscope imaging (Supplementary Fig. 10) to prevent the charge effect in accordance with the previous study [38, 53].

### ZnO nanoparticle dispersion

An air plasma chamber was used for the hydrophilic coverslip surface (5 min). We coated ZnO nanoparticles (30–40 nm, US Research nanomaterials) onto coverslips using a spin-coater twice at 3000 rpm for 30 s.

### First-principles calculations of hBN systems

The full-potential LAPW implemented in the ELK code is used for the band structure of the bulk hBN system [54]. The modified Becke-Johnson meta-generalized gradient approximation is employed to match the experimental band gap [55, 56]. We employed  $18 \times 18 \times 6$  k-grids and an 8.0 rgkmax value. We used lattice parameters of hBN as  $a = 2.502 \text{ \AA}$  and  $c = 6.617 \text{ \AA}$ .

### Instrumentation for sample characterization

The  $E_{2g}$  modes of the exfoliated hBN films were characterized using a commercial Raman spectroscopic system (Almeica XR, Nicolet) equipped with a  $50\times$  objective lens (Olympus, Mplan N) [57]. The spectra were collected for 50 s with approximately 2 mW of 532-nm laser illumination.

### Abbreviation

hBN	Hexagonal-boron nitride
CARS	Coherent anti-Stokes Raman scattering
cFE-CARS	Confocal focus-engineered coherent anti-Stokes Raman scattering
acFE-CARS	Axial-resolution-improved cFE-CARS
2D	Two-dimensional
DUV	Deep ultraviolet
SHG	Second harmonic generation
SNR	Signal-to-noise ratio
AFM	Atomic force microscopy
ND	Non-degenerate
FWM	Four-wave mixing
FE	Focus-engineered
SLM	Spatial light modulator
L-lens	Liquid lens
SDM	Short pass dichroic mirror
LDM	Long pass dichroic mirror
OL	Objective lens
GV	Galvanometric mirror
PM	Parabolic mirror
PMT	Photomultiplier tube
bg	Background
NA	Numerical aperture
ZnO	Zinc oxide
LAPW	Linearized augmented-plane-wave method

### Supplementary Information

The online version contains supplementary material available at <https://doi.org/10.1186/s43074-023-00103-6>.

**Additional file 1. Supplementary Fig. 1.** a Schematic of the polarization-resolved ND-CARS microscopy.  $\omega_1$ , 910 nm;  $\omega_2$ , 1040 nm;  $\omega_3$ , 455 nm; PMT, photomultiplier tube; Pol, polarizer. b Polarization-resolved ND-CARS images of the hBN nanosheets. The green arrow indicates the polarization directions of the incident beams. The white scale bar corresponds to 20  $\mu\text{m}$ . Three incident pulses ( $\omega_1$ , 910 nm;  $\omega_2$ , 1040 nm;  $\omega_3$ , 455 nm) were aligned in the same polarization direction and propagated to the hBN nanosheets for polarization-resolved ND-CARS microscopy (Supplementary Fig. 1a). The angle of the hBN nanosheets was rotated by  $10^\circ$  using a simple homemade rotating stage, and the emitted CARS light from the hBN nanosheets propagated to the PMT through the polarizer. The incident polarizer and the polarizer on the PMT side were set parallel. The angle shown in Supplementary Fig. 1b is the angle of the rotating state, and the precise angle was measured for Fig. 1d with the ImageJ software using the edge of the hBN nanosheets. The intensities when Pol1 and Pol2 are perpendicular are 30–60 times lower than when they are parallel (Supplementary Figs. 1b and 2). As shown in Fig. 1d and Supplementary Fig. 1b, the angle between the crystal axis of the hBN nanosheets and the incident polarization did not affect the intensity of the ND-CARS.

**Supplementary Fig. 2.** Polarization-resolved ND-CARS images of hBN nanosheets where polarizers 1 and 2 in Supplementary Fig. 1a are perpendicular to each other. The green arrow indicates the polarization directions of the incident beams. The white scale bar corresponds to 20  $\mu\text{m}$ .

**Supplementary Fig. 3.** a Bright-field and b ND-CARS image of hBN nanosheets. c Time-resolved ND-CARS intensity profile and d correspondent sequential xy-images as a function of the time overlap. The regions of d correspond to the cyan dotted box in b. e, f Correspondent AFM images as d. g AFM line profile of indicated regions in d. The green arrows indicate the polarization directions. The white scale bars correspond to 5  $\mu\text{m}$ . Supplementary Fig. 3 is the time-resolved xy-directional ND-CARS ( $\omega_1$ , 910 nm;  $\omega_2$ , 1040 nm;  $\omega_3$ , 455 nm) of hBN nanosheets in various regions. Raman-free induction decay ( $T_2/2$ ) was obtained using equation (4) in Methods [1, 2]. The dephasing time regime is well fitted with  $T_2/2 = 0.6\text{--}0.7$  ps for Raman-free induction decay in Fig. 2c, Fig. 5d and Supplementary Fig. 3c. In addition, the thicknesses of a, b, c, and d regions are 48 nm, 81 nm, 16 nm, and 41 nm, respectively, as a result of AFM measurement (Supplementary Figs. 3e–g). Therefore, the scattering time regime is independent of the thickness of hBN nanosheets (Supplementary Figs. 3c–d and 4). The Raman peak has a peak shift of about 2 to 4  $\text{cm}^{-1}$  in the monolayer and peak variation exists up to five layers [3]. Because we studied hBN nanosheets of 16 nm or larger thickness, which have more than five layers, the Raman peak and coherent phonon of hBN nanosheets are constant. Therefore, the scattering time regime is constant over the thickness of hBN nanosheets in our experiment (Supplementary Figs. 3, 4, and 5).

**Supplementary Fig. 4.** Time-resolved ND-CARS ( $\omega_1$ , 910 nm;  $\omega_2$ , 1040 nm;  $\omega_3$ , 455 nm) of various thicknesses of hBN nanosheets.

**Supplementary Fig. 5.** Time-resolved ND-CARS spectrum of arbitrary chosen hBN

nanosheets. **Supplementary Fig. 6.** a Time-resolved ND-FWM image of ZnO nanoparticles and b correspondent time-resolved intensity profile.  $\omega_1$ , 910 nm;  $\omega_2$ , 1040 nm;  $\omega_3$ , 455 nm. The green arrow indicates the polarization direction. The white scale bar corresponds to 300 nm. **Supplementary Fig. 6** shows the time-resolved ND-FWM ( $\omega_1$ , 910 nm;  $\omega_2$ , 1040 nm;  $\omega_3$ , 455 nm) imaging of the ZnO nanoparticle. The ZnO nanoparticle have a band gap of approximately 3.1 eV, and the absorption process can occur for  $\omega_1$ (910 nm) and  $\omega_3$  (455 nm) pulses [4]. Therefore, the resonant four-wave mixing process is dominant for ZnO nanoparticles [5]. Thus, the phonon vibration signal was not observed in the ZnO nanoparticles (Supplementary Fig. 6). **Supplementary Fig. 7.** The performance of cFE-CARS and acFE-CARS by measuring ZnO nanoparticles ( $\omega_1$ , 910 nm;  $\omega_2$ , 1040 nm;  $\omega_3$ , 455 nm). a Peak signal-to-background ratio (PSBR) of ND-CARS, FE-CARS, cFE-CARS, and acFE-CARS. b The vertical resolution in xy-images of cFE-CARS and acFE-CARS. c The axial line profiles of cFE-CARS and acFE-CARS region correspond to Figs. 3d–e. The green arrow in a indicates the polarization directions. The white scale bar corresponds to 300 nm. The PSBR value is defined as  $(I_p - I_{bg})/I_{bg}$ , where  $I_p$  is the average of the central peak and  $I_{bg}$  is the average of the background area [6, 7]. The same ZnO nanoparticles were imaged for the PSBR calculations using various CARS modes (Supplementary Fig. 7a, inset). In addition, the central peak was used for the PSBR calculation. As shown in Supplementary Fig. 7, the contrasts of FE-CARS and cFE-CARS were approximately 5.7 and approximately 11.3 times lower than that of ND-CARS, respectively. However, the contrast of acFE-CARS was only approximately 3.0 times lower than that of ND-CARS and approximately 3.8 times higher than that of cFE-CARS. **Supplementary Fig. 7b** shows the lateral resolution of the cFE-CARS and acFE-CARS. The CARS intensity was proportional to the square of the nanoparticle diameter [8, 9]. Therefore, acFE-CARS can image smaller-diameter nanoparticles than cFE-CARS because of the higher contrast of acFE-CARS. To compare the maximum performance of the lateral resolution of cFE-CARS and acFE-CARS, we measured the ZnO nanoparticles with a small FWHM in each imaging mode. The xy-resolution of cFE-CARS was approximately 96 nm, and that of acFE-CARS was approximately 120 nm. **Supplementary Fig. 7c** shows the z-directional line profile of the PSF of cFE-CARS and acFE-CARS in Figs. 3c–d. **Figs. 3b–d** shows the PSF using the small imageable ZnO nanoparticles with cFE-CARS. To show the overall performance of acFE-CARS, we used a smaller ZnO nanoparticle in Fig. 3e than in Fig. 3b–d, in which cFE-CARS cannot be imaged. The FWHM of the z-directional PSF of acFE-CARS was approximately 499 nm, and that of cFE-CARS was approximately 1397 nm. Consequently, the lateral resolution of acFE-CARS is approximately 1.25 times lower than that of cFE-CARS. However, the axial resolution and contrast of acFE-CARS are approximately 2.8 and approximately 3.8 times higher than cFE-CARS, respectively. Therefore, acFE-CARS is applicable for imaging various complex systems with high resolution. **Supplementary Fig. 8.** a ND-CARS, b acFE-CARS, and c AFM image, and corresponding line profiles d–e. a and b are mean filtered images. e Edge resolution is fitted with the gaussian cumulative distribution function. Edge resolution is measured with a distance between 10% and 90% of intensity. The green arrows indicate the polarization directions. The white scale bars correspond to 1  $\mu$ m. Another example of resolution improvement using acFE-CARS is shown in **Supplementary Fig. 8**, which consistently showed an approximately two times enhancement in the lateral resolution (**Supplementary Fig. 8e**). The results are shown (**Supplementary Figs. 8d–e**) and compared with the corresponding line profile from the AFM image in **Supplementary Fig. 8c**. We verified the visualization capability of acFE-CARS on the gaps between different flakes (a lines). In **Supplementary Fig. 8d**, the discontinuity of the flake-to-flake gap is more explicitly featured in the acFE-CARS than in the ND-CARS microscopy images, with contrasts that are approximately four times deeper and three times wider. In addition, the gap between distinct hBN nanosheets was verified by AFM (**Supplementary Figs. 8c–d**) and SEM (**Supplementary Fig. 10**, cyan arrow). **Supplementary Fig. 9** shows the ND-CARS (**Supplementary Fig. 9a**) and acFE-CARS (**Supplementary Fig. 9b**) images identical to those in **Supplementary Figs. 8a–9b**, but with a mean-filtering process. **Supplementary Figs. 9c–d** compare changes in the line profiles (a and b) in the absence and presence of mean filtering, showing an improvement in the SNR of more than 9. The gap a was more distinctively resolved using mean filtering. The normal cumulative distribution function ( $\Phi$ ) is used for fitting function of the edge line profiles [6, 9]. We employed the distance between 10% and 90% of the fitted function ( $2.564\omega$ ) to determine edge resolution. The edge resolutions of ND-CARS and acFE-CARS are 239.412.8 nm, and 105.825.7 nm, respectively (**Supplementary Fig. 8e**). In addition, we capped monolayer CVD graphene onto the hBN nanosheets to prevent the charge effect for SEM imaging after the entire CARS experiment (**Supplementary Fig. 10**). Field-emission SEM (Hitachi, SU8020) was used to visualize the graphene-covered hBN nanosheets after CARS imaging at an accelerating voltage of 3 keV, with exposure to a 10  $\mu$ A beam current. The thicknesses of the atomically thin hBN crystals were determined by atomic force microscopy (XE-150, Park system) using an NSC36/Rc-Au tip as a probe. **Supplementary Fig. 9.** a ND-CARS, and b acFE-CARS image of hBN nanosheets. The equivalent region with **Supplementary Figs. 8a–c**, which are mean filtered images. c, d Comparison between with and without mean filtering of ND-CARS c and cFE-CARS d. The  $\alpha$ , and  $\beta$  mean regions indicated in **Supplementary Figs. 8a–c**. The green arrow indicates the polarization direction. The white scale bars correspond to 1  $\mu$ m. **Supplementary Fig. 10.** The SEM images of hBN nanosheets covered by graphene which correspond to the region in **Supplementary Fig. 8**. The white scale bars correspond to a 20 , b 10 , c 1 , d 0.5. **Supplementary Fig. 11.** a The AFM image of Fig. 4a region. b–d AFM line profiles of hBN flakes of Figs. 4b–c (b, 19 nm; c, 72 nm; d 104 nm). The white scale bar corresponds to 10 m. **Supplementary Fig. 12.** a Bright-field image and b acFE-CARS image of hBN flakes. The z-directional c–d ND-CARS and e–f acFE-CARS image of hBN flakes. The regions are indicated in b. g–h The z-directional line profiles of ND-CARS and acFE-CARS of hBN flakes. The corresponding region is indicated in c and d. The regions in c, e correspond to g; d, f correspond to h. The green arrow indicates the polarization direction. The white scale bars correspond to b 10 m and c 5 m. **Supplementary Fig. 12** shows z-directional images of ND-CARS and acFE-CARS. Owing to the polarization direction of the incident beams and the thickness of hBN nanosheets, the axial resolution varies depending on the z-scanning direction, even for the same thickness of hBN nanosheet. Thus, the axial resolution of acFE-CARS on hBN nanosheets can be determined at about 350 to 550 nm (Fig. 4g and **Supplementary Figs. 12g–h**). **Supplementary Fig. 13.** Time-resolved axial ND-CARS images of hBN nanosheets. a The ND-CARS images of hBN nanosheets. b Time-resolved axial ND-CARS intensity profile and c correspondent sequential axial images as a function of the time overlap. The region c is



depth imaging performed in the axial direction along the dotted cyan line of the a. The green arrow indicates the polarization direction. The green dotted box is measured for the time-resolved axial ND-CARS background intensity profile in Fig. 5d. Supplementary Figs. 13b–c show time-resolved axial ND-CARS dynamic imaging. The time-resolved study was performed by z-directional scanning of the cyan dotted line in Supplementary Fig. 13a. From the time-resolved intensity profiles of the bright region corresponding to hBN nanosheets (i), phonon vibration was observed in the hBN nanosheet region. However, the region decays toward coverslip (ii) decays. Therefore, region (ii) can be determined as the background signals from immersion oil or coverslips, which are not CARS signals from the hBN nanosheet. **Supplementary Fig. 14.** Schematic diagram used for axial resolution calculation.

#### Acknowledgements

Not applicable at this moment.

#### Authors' contributions

G.L. and H.K. made an original concept of experimental scheme. G.L. lead the experiments, prepare for the figure sets and wrote the manuscript. K.M.J. performed the calculation and reviewed the manuscript. J.P. assisted the experimental setup and funding. J.D.L. participated in calculation and theoretical conceptualization. V.R. reviewed and edited the manuscript. H.K. wrote the original draft, investigated, and finalized the manuscript with G.L.

#### Funding

This study was supported by the National Research Foundation of Korea (2023R1A2C100531711). H.K. also acknowledges support from the DGIST R&D programs (22-CoENT-01 and 22-BT-06) funded by the Ministry of Science and ICT. V.R. acknowledges support from Department of Science and Technology (DST) Indo-Korea joint research project (INT/Korea/P-44).

#### Availability of data and materials

The relevant data of this study are available from the corresponding authors on reasonable request.

#### Declarations

##### Ethics approval and consent to participate

There is no ethics issue for this paper.

##### Consent for publication

All authors agreed to publish this paper.

##### Competing interests

The authors declare that they have no competing interests.

Received: 8 January 2023 Revised: 11 July 2023 Accepted: 2 August 2023

Published online: 28 August 2023

#### References

1. Caldwell JD, Aharonovich I, Cassabois G, Edgar JH, Gil B. Photonics with hexagonal boron nitride. *Nat Rev Mater*. 2019;4:552–67. <https://doi.org/10.1038/s41578-019-0124-1>.
2. Withers F, Del Pozo-Zamudio O, Mishchenko A, Rooney AP, Gholinia A, Watanabe K, et al. Light-emitting diodes by band-structure engineering in van der Waals heterostructures. *Nat Mater*. 2015;14:301–6. <https://doi.org/10.1038/nmat4205>.
3. Xu S, Wu Z, Lu H, Han Y, Long G, Chen X, et al. Universal low-temperature Ohmic contacts for quantum transport in transition metal dichalcogenides. *2DMater*. 2016;3:021007. <https://doi.org/10.1088/2053-1583/3/2/021007>.
4. Dean CR, Young AF, Meric I, Lee C, Wang L, Sorgenfrei S, et al. Boron nitride substrates for high-quality graphene electronics. *Nat Nanotechnol*. 2010;5:722–6. <https://doi.org/10.1038/nnano.2010.172>.
5. Wang L, Meric I, Huang PY, Gao Q, Gao Y, Tran H, et al. One-dimensional electrical contact to a two-dimensional material. *Science*. 2013;342:614–7. <https://doi.org/10.1126/science.1244358>.
6. Jia Y, Zhao H, Guo Q, Wang X, Wang H, Xia F. Tunable plasmon-phonon polaritons in layered graphene-hexagonal boron nitride heterostructures. *ACS Photonics*. 2015;2:907–12. <https://doi.org/10.1021/acsphotonics.5b00099>.
7. Basov DN, Fogler MM, García de Abajo FJ. Polaritons in van der Waals materials. *Science*. 2016;354:6309. <https://doi.org/10.1126/science.aag1992>.
8. Dai S, Ma Q, Liu MK, Andersen T, Fei Z, Goldflam MD, et al. Graphene on hexagonal boron nitride as a tunable hyperbolic metamaterial. *Nat Nanotechnol*. 2015;10:682–6. <https://doi.org/10.1038/nnano.2015.131>.
9. Low T, Chaves A, Caldwell JD, Kumar A, Fang NX, Avouris P, et al. Polaritons in layered two-dimensional materials. *Nat Mater*. 2017;16:182–94. <https://doi.org/10.1038/nmat4792>.
10. Bourrellier R, Meuret S, Tararan A, Stéphan O, Kociak M, Tizei LHG, Zibelli A. Bright UV single photon emission at point defects in h-BN. *Nano Lett*. 2016;16:4317–21. <https://doi.org/10.1021/acs.nanolett.6b01368>.
11. Kim S, Frösch JE, Christian J, Straw M, Bishop J, Totonjian D, et al. Photonic crystal cavities from hexagonal boron nitride. *Nat Commun*. 2018;9:2623. <https://doi.org/10.1038/s41467-018-05117-4>.
12. Song S-B, Yoon S, Kim SY, Yang S, Seo S-Y, Cha S, et al. Deep-ultraviolet electroluminescence and photocurrent generation in graphene/hBN/graphene heterostructures. *Nat Commun*. 2021;12:7134. <https://doi.org/10.1038/s41467-021-27524-w>.

13. Tran TT, Bray K, Ford MJ, Toth M, Aharonovich I. Quantum emission from hexagonal boron nitride monolayers. *Nat Nanotechnol.* 2016;11:37–41. <https://doi.org/10.1038/nnano.2015.242>.
14. Tran TT, Elbadawi C, Totonjian D, Lobo CJ, Grosso G, Moon H, et al. Robust multicolor single photon emission from point defects in hexagonal boron nitride. *ACS Nano.* 2016;10:7331–8. <https://doi.org/10.1021/acs.nano.6b03602>.
15. Jungwirth NR, Calderon B, Ji Y, Spencer MG, Flatté ME, Fuchs GD. Temperature dependence of wavelength selectable zero-phonon emission from single defects in hexagonal boron nitride. *Nano Lett.* 2016;16:6052–7. <https://doi.org/10.1021/acs.nanolett.6b01987>.
16. Trovatiello C, Marini A, Xu X, Lee C, Liu F, Curreli N, et al. Optical parametric amplification by monolayer transition metal dichalcogenides. *Nat Photonics.* 2021;15:6–10. <https://doi.org/10.1038/s41566-020-00728-0>.
17. Li Y, Rao Y, Mak KF, You Y, Wang S, Dean CR, Heinz TF. Probing symmetry properties of few-layer MoS<sub>2</sub> and h-BN by optical second-harmonic generation. *Nano Lett.* 2013;13:3329–33. <https://doi.org/10.1021/nl401561r>.
18. Watanabe K, Taniguchi T, Kanda H. Direct-bandgap properties and evidence for ultraviolet lasing of hexagonal boron nitride single crystal. *Nat Mater.* 2004;3:404–9. <https://doi.org/10.1038/nmat1134>.
19. Miseur L, Brasse G, Pierret A, Maine S, Attal-Tretout B, Ducastelle F, et al. Exciton optical transitions in a hexagonal boron nitride single crystal. *Phys Stat Solidi Rapid Res Lett.* 2011;5:214–6. <https://doi.org/10.1002/pssr.201105190>.
20. Cassaboïs G, Valvin P, Gil B. Hexagonal boron nitride is an indirect bandgap semiconductor. *Nat Photonics.* 2016;10:262–6. <https://doi.org/10.1038/nphoton.2015.277>.
21. Popkova AA, Antropov IM, Frösch JE, Kim S, Aharonovich I, Bessonov VO, et al. Optical third-harmonic generation in hexagonal boron nitride thin films. *ACS Photonics.* 2021;8:824–31. <https://doi.org/10.1021/acsphotonics.0c01759>.
22. Ling J, Miao X, Sun Y, Feng Y, Zhang L, Sun Z, Ji M. Vibrational imaging and quantification of two-dimensional hexagonal boron nitride with stimulated raman scattering. *ACS Nano.* 2019;13:14033–40. <https://doi.org/10.1021/acsnano.9b06337>.
23. Lafetà L, Cadore AR, Mendes-De-Sa TG, Watanabe K, Taniguchi T, Campos LC, et al. Anomalous nonlinear optical response of graphene near phonon resonances. *Nano Lett.* 2017;17:3447–51. <https://doi.org/10.1021/acs.nanolett.7b00329>.
24. Armstrong JA, Bloembergen N, Ducuing J, Pershan PS. Interactions between light waves in a nonlinear dielectric. *Phys Rev.* 1962;127:1918–39. <https://doi.org/10.1103/PhysRev.127.1918>.
25. Cheng J-X, Volkmer A, Xie XS. Theoretical and experimental characterization of coherent anti-Stokes Raman scattering microscopy. *J Opt Soc Am B.* 2002;19:1363–75. <https://doi.org/10.1364/josab.19.001363>.
26. Hempel F, Reitzig S, Rüsing M, Eng LM. Broadband coherent anti-stokes raman scattering for crystalline materials. *Phys Rev B.* 2021;104:224308. <https://doi.org/10.1103/PhysRevB.104.224308>.
27. Dhakal KP, Kim H, Lee S, Kim Y, Lee JD, Ahn JH. Probing the upper band gap of atomic rhenium disulfide layers. *Light Sci Appl.* 2018;7:98. <https://doi.org/10.1038/s41377-018-0100-3>.
28. Hendry E, Hale PJ, Moger J, Savchenko AK, Mikhailov SA. Coherent nonlinear optical response of graphene. *Phys Rev Lett.* 2010;105:097401. <https://doi.org/10.1103/PhysRevLett.105.097401>.
29. Lotem H, Lynch RT, Bloembergen N. Interference between Raman resonances in four-wave difference mixing. *Phys Rev A.* 1976;14:1748–55. <https://doi.org/10.1103/physreva.14.1748>.
30. Gorbachev RV, Riaz I, Nair RR, Jalil R, Britnell L, Belle BD, et al. Hunting for monolayer boron nitride: optical and Raman signatures. *Small.* 2011;7:465–8. <https://doi.org/10.1002/sml.201001628>.
31. Sönnichsen C, Franzl T, Wilk T, von Plessen G, Feldmann J, Wilson O, Mulvaney P. Drastic reduction of plasmon damping in gold nanorods. *Phys Rev Lett.* 2002;88:077402. <https://doi.org/10.1103/PhysRevLett.88.077402>.
32. Lee YJ, Cicerone MT. Vibrational dephasing time imaging by time-resolved broadband coherent anti-Stokes Raman scattering microscopy. *Appl Phys Lett.* 2008;92:041108. <https://doi.org/10.1063/1.2838750>.
33. Lee YJ, Parekh SH, Fagan JA, Cicerone MT. Phonon dephasing and population decay dynamics of the G-band of semiconducting single-wall carbon nanotubes. *Phys Rev B.* 2010;82:165432. <https://doi.org/10.1103/PhysRevB.82.165432>.
34. Koivisto J, Myllyperkiö P, Pettersson M. Time-resolved coherent anti-stokes raman scattering of graphene: dephasing dynamics of optical phonon. *J Phys Chem Lett.* 2017;8:4108–12. <https://doi.org/10.1021/acs.jpclett.7b01711>.
35. Xu Q-H, Ma Y-Z, Fleming GR. Heterodyne detected transient grating spectroscopy in resonant and non-resonant systems using a simplified diffractive optics method. *Chem Phys Lett.* 2001;338:254–62. [https://doi.org/10.1016/S0009-2614\(01\)00281-0](https://doi.org/10.1016/S0009-2614(01)00281-0).
36. Seferyan HY, Nasr MB, Senekerimyan V, Zadoyan R, Collins P, Apkarian VA. Transient grating measurements of excitonic dynamics in single-walled carbon nanotubes: The dark excitonic bottleneck. *Nano Lett.* 2006;6:1757–60. <https://doi.org/10.1021/nl061646d>.
37. Zeytunyan A, Crampton KT, Zadoyan R, Apkarian VA. Supercontinuum-based three-color three-pulse time-resolved coherent anti-Stokes Raman scattering. *Opt Express.* 2015;23:24019–28. <https://doi.org/10.1364/OE.23.024019>.
38. Lee G, Jyothsna KM, Lim H, Park J, Lee J, Raghunathan V, Kim H. Sub 100 nm resolution confocal focus-engineered coherent anti-Stokes Raman scattering microscopy under non-degenerate pumping condition. *Opt Lasers Eng.* 2022;158:107142. <https://doi.org/10.1016/j.optlaseng.2022.107142>.
39. Beams R, Woodcock JW, Gilman JW, Stranick SJ. Phase mask-based multimodal superresolution microscopy. *Photonics.* 2017;4:39. <https://doi.org/10.3390/photonics4030039>.
40. Kim H, Bryant GW, Stranick SJ. Superresolution four-wave mixing microscopy. *Opt Express.* 2012;20:6042–51. <https://doi.org/10.1364/OE.20.006042>.
41. Hashimoto M, Araki T. Three-dimensional transfer functions of coherent anti-Stokes Raman scattering microscopy. *J Opt Soc Am A.* 2001;18:771–6. <https://doi.org/10.1364/JOSAA.18.000771>.
42. Gong L, Zheng W, Ma Y, Huang Z. Higher-order coherent anti-Stokes Raman scattering microscopy realizes label-free super-resolution vibrational imaging. *Nat Photonics.* 2020;14:115–22. <https://doi.org/10.1038/s41566-019-0535-y>.
43. Mehravar S, Cromey B, Kieu K. Characterization of multiphoton microscopes by the nonlinear knife-edge technique. *Appl Opt.* 2020;59:G219–24. <https://doi.org/10.1364/AO.391881>.

44. Brizuela F, Wang Y, Brewer CA, Pedaci F, Chao W, Anderson EH, et al. Microscopy of extreme ultraviolet lithography masks with 13.2 nm tabletop laser illumination. *Opt Lett*. 2009;34:271–3. <https://doi.org/10.1364/ol.34.000271>.
45. Novotny L, Hecht B. Principles of nano-optics. Ch. 4. Cambridge University Press; 2006.
46. Latychevskaia T. Lateral and axial resolution criteria in incoherent and coherent optics and holography, near- and far-field regimes. *Appl Opt*. 2019;58:3597–603. <https://doi.org/10.1364/AO.58.003597>.
47. Potma EO, Evans CL, Xie XS. Heterodyne coherent anti-Stokes Raman scattering (CARS) imaging. *Opt Lett*. 2006;31:241–3. <https://doi.org/10.1364/ol.31.000241>.
48. Freudiger CW, Min W, Saar BG, Lu S, Holtom GR, He C, et al. Label-free biomedical imaging with high sensitivity by stimulated Raman scattering microscopy. *Science*. 2008;322:1857–61. <https://doi.org/10.1126/science.1165758>.
49. Virga A, Ferrante C, Batignani G, De Fazio D, Nunn ADG, Ferrari AC, et al. Coherent anti-Stokes Raman spectroscopy of single and multi-layer graphene. *Nat Commun*. 2019;10:3658. <https://doi.org/10.1038/s41467-019-11165-1>.
50. Evans CL, Xie XS. Coherent anti-stokes Raman scattering microscopy: chemical imaging for biology and medicine. *Annu Rev Anal Chem*. 2008;1:883–909. <https://doi.org/10.1146/annurev.anchem.1.031207.112754>.
51. Ariunbold GO, Altangerel N. Quantitative interpretation of time-resolved coherent anti-Stokes Raman spectroscopy with all Gaussian pulses. *J Raman Spectrosc*. 2017;48:104–7. <https://doi.org/10.1002/jrs.4987>.
52. Zhang X, Li Y, Mu W, Bai W, Sun X, Zhao M, et al. Advanced tape-exfoliated method for preparing large-area 2D monolayers: a review. *2D Mater*. 2021;8:032002.
53. Song J, Kam F-Y, Png R-Q, Seah W-L, Zhuo J-M, Lim G-K, et al. A general method for transferring graphene onto soft surfaces. *Nat Nanotechnol*. 2013;8:356–62. <https://doi.org/10.1038/nnano.2013.63>.
54. The Elk Code. <https://elk.sourceforge.io/>.
55. Tran F, Blaha P. Accurate band gaps of semiconductors and insulators with a semilocal exchange-correlation potential. *Phys Rev Lett*. 2009;102:226401. <https://doi.org/10.1103/PhysRevLett.102.226401>.
56. Schuster R, Habenicht C, Ahmad M, Knupfer M, Büchner B. Direct observation of the lowest indirect exciton state in the bulk of hexagonal boron nitride. *Phys Rev B*. 2018;97:041201(R). <https://doi.org/10.1103/PhysRevB.97.041201>.
57. Kim J-H, Van Le Q, Nguyen TP, Lee TH, Jang HW, Yun WS, et al. Graphene-mediated enhanced Raman scattering and coherent light lasing from CsPbI<sub>3</sub> perovskite nanorods. *Nano Energy*. 2020;70:104497. <https://doi.org/10.1016/j.nanoen.2020.104497>.

## Publisher's Note

Springer Nature remains neutral with regard to jurisdictional claims in published maps and institutional affiliations.

Submit your manuscript to a SpringerOpen<sup>®</sup> journal and benefit from:

- Convenient online submission
- Rigorous peer review
- Open access: articles freely available online
- High visibility within the field
- Retaining the copyright to your article

---

Submit your next manuscript at ► [springeropen.com](https://www.springeropen.com)

---